ACS OMEGA

Open Access

http://pubs.acs.org/journal/acsodf

Article

Controlling the Formation of Polyhedral Block Copolymer Nanoparticles: Insights from Process Variables and Dynamic Modeling

Edgar Avalos,* Takashi Teramoto, Yutaro Hirai, Hiroshi Yabu,* and Yasumasa Nishiura*

Cite This: *ACS Omega* 2024, 9, 17276−17288

Read Online

ACCESS | Metrics & More | Article Recommendations | Supporting Information

ABSTRACT: This study delves into the formation of nanoscale polyhedral block copolymer particles (PBCPs) exhibiting cubic, octahedral, and variant geometries. These structures represent a pioneering class that has never been fabricated previously. PBCP features distinct variations in curvature on the outer surface, aligning with the edges and corners of polyhedral shapes. This characteristic sharply contrasts with previous block copolymers (BCPs), which displayed a smooth spherical surface. The emergence of these cornered morphologies presents an intriguing and counterintuitive phenomenon and is linked to process parameters, such as evaporation rates and initial concentration, while keeping other variables constant. Using a system of coupled Cahn−Hillard (CCH) equations, we uncover the mechanisms driving polyhedral particle formation, emphasizing the importance of controlling relaxation parameters for shape variable u and microphase separation v. This unconventional approach, differing from traditional steepest descent method, allows for precise control and diverse polyhedral particle generation. Accelerating the shape variable u proves crucial for expediting precipitation and aligns with experimental observations. Employing the above theoretical model, we achieve shape predictions for particles and the microphase separation within them, which overcomes the limitations of ab initio computations. Additionally, a numerical stability analysis discerns the transient nature versus local minimizer characteristics. Overall, our findings contribute to understanding the complex interplay between process variables and the morphology of polyhedral BCP nanoparticles.

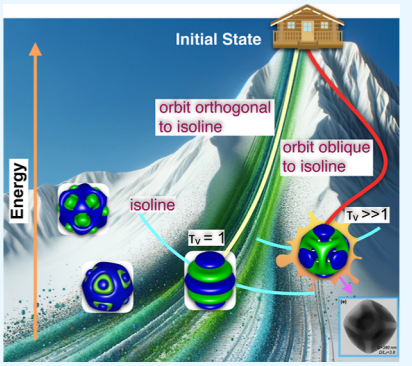

1. INTRODUCTION

The study of phase separation in block copolymers (BCPs) within confined spaces has emerged as a captivating research frontier, largely attributed to the striking distinctions between confined and bulk morphologies. Notably, extensive investigations have been dedicated to one-dimensional (1D) confinement[1−5] within thin films and two-dimensional (2D) confinement[6] within anodic aluminum oxide templates.[7] Phase-separation structures in three-dimensional (3D) confined spaces have attracted much attention as well and various structures different from the bulk state have been reported.[8−10] Typical examples of 3D confined space entities are BCP nanoparticles.[11−14] Additionally, extensive research has been conducted on a wide range of cylindrical confinement scenarios.[7,15−34] Onion, ellipsoid, and slightly deformed shapes associated with these two morphologies are most frequently observed in experiments and are well-studied.[35,36] A distinguishing feature of these particles is the smooth, spherical shape of their associated 2D boundaries without edges and corners. This holds true even when the internal structure, such as k-noids, exhibits complexity.

This paper embarks on a comprehensive exploration of BCP nanoparticles, specifically those adopting polyhedral shapes such as cubes, octahedra, and their derivatives that have never been fabricated before. A notable departure from previous BCPs lies in the pronounced variation of curvature on the outer surface, closely aligning with the edges and corners of polyhedral shapes. A pivotal revelation lies in the profound influence of process variables, such as evaporation and precipitation rates, on the formation of these polyhedral particles, even when other experimental parameters, including composition and molecular weights, remain fixed. Hence, this study delves deeply into the intricate interplay between these process variables and the resultant polyhedral particle shapes from a theoretical standpoint through the application of a mathematical model.

Various factors contribute to the morphological diversity of BCP nanoparticles.[37] For instance, symmetric composition of polystyrene-*block*-polyisoprene (PS-*b*-PI) in solution often results in nanoparticles with layered morphology,[38] while asymmetric compositions lead to an array of configura-

Received: December 23, 2023
Revised: February 20, 2024
Accepted: February 26, 2024
Published: March 29, 2024

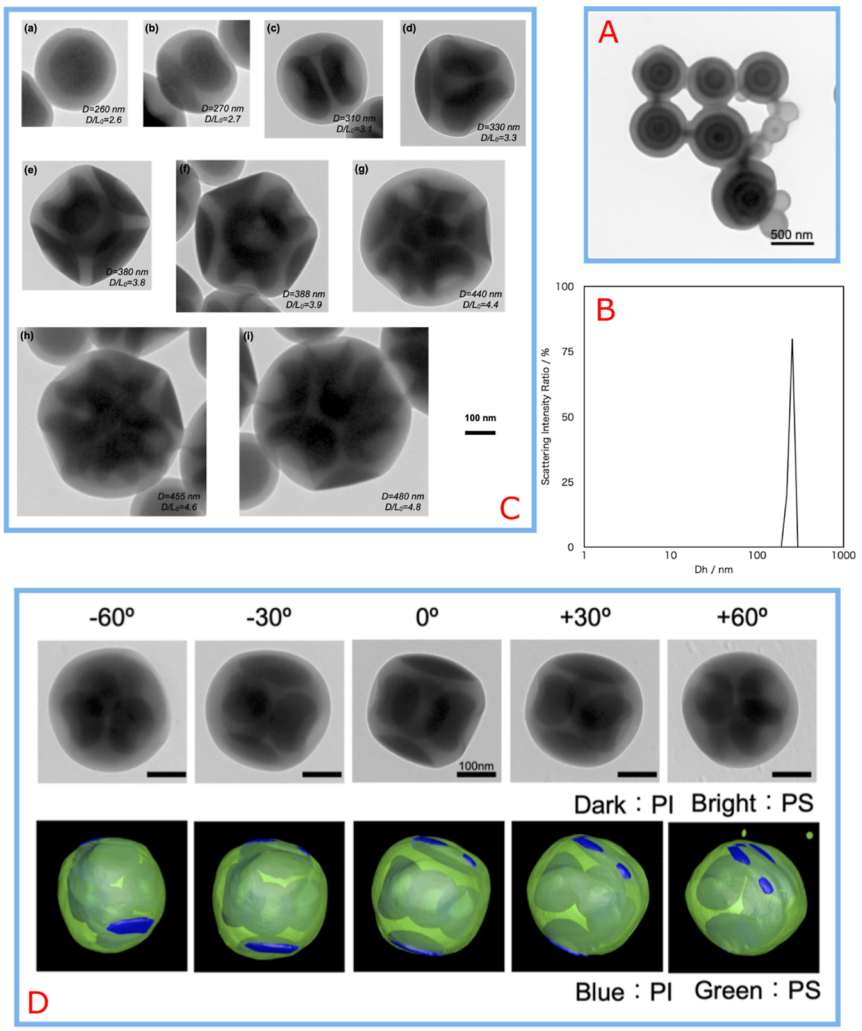

Figure 1. (A) TEM image displaying PS-*b*-PI particles obtained from a particle dispersion prepared using a 1.0 mg/mL THF solution. (B) Dynamic light scattering (DLS) measurement results for the aqueous dispersion of particles obtained from a 1.0 mg/mL solution of PS-*b*-PI. (C) TEM images showcasing PS-*b*-PI particles of various sizes. Insets within each image provide size and D/L_0 values for the respective particles. The scale bar represents 100 nm. (D) Upper row: tilted TEM images illustrating PI and PS phases with dark and bright contrasts, respectively. Bottom row: tilted electron tomography (ET) images displaying PI and PS phases as blue and green, respectively, for PS-*b*-PI particles with a D/L_0 value of 3.8.

tions.[35,39,40] A diverse array of recent investigations has delved into the self-assembly of BCP in 3D space.[12−14,36,41] One notable study delves into the factors that influence nanostructures during the confined self-assembly of BCP within emulsion droplets. The focus is specifically on the spatial arrangement of inorganic nanoparticles on the resulting scaffolds.[12] Another study explores the 3D confined assembly of BCPs, highlighting its potential for efficiently creating unconventional polymer materials with desired shapes and internal nanostructures. This study systematically summarizes key experimental parameters, including evaporation, that influence the assembly structures.[13] In the realm of 3D soft confinement, a semicrystalline triblock terpolymer self-assembles into frustrated multicompartment nanoparticles.[14] Furthermore, the exploration of controlling metastable states during chemical reduction is undertaken to fabricate multimetallic mesoporous nanospheres. This introduces a novel aspect in material synthesis by tuning both compositions and mesopore morphology.[41] The design of BCP nanoparticles with stimuli-responsive reversible morphology is also presented.[36] This design facilitates dynamic transformations between onion, layered, and ellipsoidal structures. The comprehensive examination of polymers manifesting intricate configurations, such as polymer brushes[42] and terpolymer-based nanoparticles,[43] remains notably constrained within the existing literature on chemical synthesis and assembly behavior. Manipulating molecular weights and chain rigidities within confined BCP nanoparticles induces a transition from onion-like concentric structures to striped ellipsoids. This transition is attributed to the elevated entropic penalty associated with bending lamella domains in BCP particles with large molecular weights.[35,39,40,44] Furthermore, temperature variations have been shown to drive transformations, with particles transitioning from layered to onion-like morphologies when the temperature of annealing increased from 20 to 40 °C.[45] Additionally, microwave annealing has proven effective in accelerating phase separation into thermally stable structures.[46]

A myriad of experimental conditions affect the shape of particles. For instance, ultraviolet and visible light exposure influence the amphiphilicity of the surfactants to different polymers blocks causing changes of the shape in nanoparticles

https://doi.org/10.1021/acsomega.3c10302
ACS Omega 2024, 9, 17276−17288

from onion-shaped spherical particles to striped ellipsoids and, ultimately, to inverse onion-like particles.[47] The rate of solvent evaporation, a dynamic process, remarkably affects final morphologies,[48] adding an unexpected layer of complexity to the origin of polyhedral particles. In contrast to the inherently spherical or spherical-like particles, the emergence of polyhedral BCP morphologies necessitates the control of external factors, here referred to as process variables. Recently there is an increasing interest in developing nanoparticles with polyhedral structure. Although there are some studies involving membranes and shells with polyhedral shape,[49−51] faceted polymersomes[52,53] and BCP-directed morphogenesis of polyhedral metal nanoparticles,[54] to the best of our knowledge there are not exhaustive studies of BCP particles with nonspherical shape.

Several computational investigations on BCP systems subjected to spherical confinement have been documented in prior studies.[55−68] Numerous attempts to understand BCP particle morphological transformations via simulations have employed coupled Cahn−Hillard (CCH) equations, successfully guiding nanoparticle design.[69] In ref 70, the authors used the CCH to transform ellipsoidal BCP nanoparticles into onion-like spheres by modulating the parameters, accommodating temperature-induced changes during heating. Manipulating solvent interactions with BCP segments, as seen in ternary blended polymers[71] plays a vital role in nanoparticle morphology, structure, and properties. Precisely adjusting solvent preferences for specific BCP segments allows precise control over exposed surface areas in nanoparticles,[69] holding potential for diverse applications, including drug release modulation in nanomedicine.

Typically, researchers seek BCP morphologies by finding the steepest descent direction of an appropriate free energy, yielding a set of model equations describing different minimizers based on energy functional parameters and initial conditions (ICs). In contrast, this work introduces an alternative approach using the CCH model with time-relaxation parameters (τ_u and τ_v) to dynamically model nonspherical BCP particles. The relaxation parameter τ_v, governing nonspherical morphologies, emerges as a key factor shaping final morphology of the particle. This novel approach connects dynamic processes to nanoparticle morphology, aligning computational findings with experimental evidence. The key distinction between these approaches lies in how resulting morphologies are determined. In the first, commonly used approach, morphologies depend on the parameters of the energy functional, while in the second approach, the ratio of the speed factors in front of the time-derivatives of the Euler−Lagrange equations, which have nothing to do with inherent chemical parameters, plays a crucial role to find a right regime for polygonal morphologies.

Our aim is to elucidate the relationship between dynamic processes governed by τ_v and the final morphology of the particle. We explore how speed factors influence both transient and final-stage morphologies, consistent with experimental evidence. In a field dominated by spherical or quasi-spherical particles, this study provides fresh insights into nonspherical BCP nanoparticle formation and governing principles. Through dynamic modeling and process variable control, we illuminate previously uncharted territory in BCP nanoparticle research, opening avenues for innovative applications in drug delivery, materials science, and beyond.

2. RESULTS

2.1. Experimental Results. The Figure 1A shows the transmission electron microscopy (TEM) image of the particles prepared in a 40 °C water bath. The TEM images show the formation of spherical nanoparticles with an onion-like phase separation structure,[35,38,72] which is similar to the phase separation structure observed in the unconfined nanoparticles.[35]

In what follows we will present the results for the case where reduced pressure is used to produce the particles unlike a conventional setting as in Figure 1A. The results of DLS measurements in Figure 1B show that the resulting particles have a unimodal size distribution. Although the size distribution is sufficiently narrow, it contains particles of different sizes within it. Figure 1C shows the TEM images of the obtained particles with different sizes arranged from the smallest to the largest. The smallest particle size is 260 nm and the largest size is 480 nm. As depicted in Figure 1B, particle size distributions become apparent due to the particles forming through a spontaneous precipitation process. The size and distribution of these particles are influenced by factors such as the concentration of the polymer solution, the mixing ratio between the polymer solution and water, and evaporation speed, as discussed in the literature.[73]

In this report, we investigate the effects of 3D confinement on BCP phase separation. We selected particles of various sizes and observed their internal structures using TEM to uncover the relationship between particle size and internal structures. The normalized size ratio, D/L_0, representing the ratio between the particle size, D, and the periodicity of BCP phase separation in bulk, L_0, serves as a crucial metric for gauging the extent to which the BCP is confined within the particles. This value plays an important role in controlling the phase-separated structures of the BCP under 3D confinement.[8] The size of each particle and the value of D/L_0 are shown in Figure 1C on the bottom right. As the particle size increases, the value of D/L_0 also increases. Figure 1C-a shows a TEM image of the smallest particle with a size of 260 nm and D/L_0 = 2.6. The particles are spherical in shape and form a core−shell structure with the OsO_4-stained PI phase as the core and the unstained PS phase as the shell. It is reasonable that the core−shell structure can be obtained from the almost 1:1 BCP used in this experiment. And the reason for this is that BCPs exhibiting lamellar structures in the bulk, also form uniaxially stacked lamellar structures and onion-like microphase separated structures in the bulk.

On the other hand, gradually increasing the particle size and D/L_0, transforms the inner PI phase of the particle into a bowl-shaped structure, as it is shown in Figure 1C-b,c. Similarly, the shape of the facet of particle changed to a triangular shape according to the bowl indentation as it is shown in Figure 1C-d. As the size of the particles increased, the TEM images showed quadrangular (Figure 1C-e) and pentagonal (Figure 1C-f) structures, suggesting that the actual structure is polyhedral, as the TEM images were obtained using transmitted electrons. At larger grain sizes, polyhedral particles with a complex distribution of bowl-shaped PI phases were formed (Figure 1C-g−i).

Figure 1D shows ET images of the nanoparticles with D/L_0 = 3.8. The upper panel shows TEM images obtained by rotating the sample stage from −60 to +60° in 30° steps, and the lower panel shows ET images corresponding to the upper

https://doi.org/10.1021/acsomega.3c10302
ACS Omega 2024, 9, 17276−17288

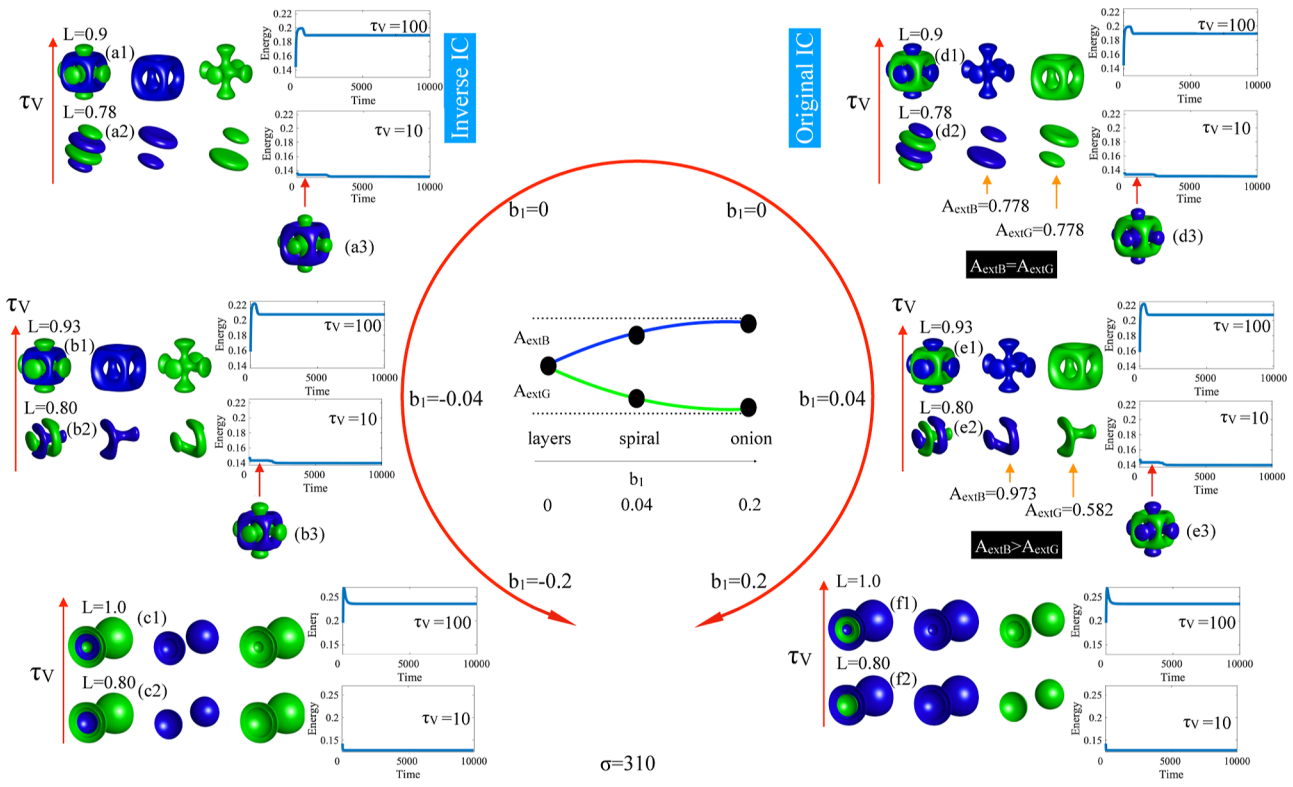

Figure 2. Diagram with a variety of morphologies for different values of the interaction with the solvent with appropriate system size. The parameters of this figure are in the Appendix A.

panel obtained by tilting the sample stage ±60° in 1° steps. The 0° TEM image shows the formation of a plate-like PI phase at the top and bottom of the nanoparticles, and four bowl-shaped phase-separated structures inside the particle. From the ±60 to ±30° images, four bowl-shaped structures were observed in the central part, each with a concave central part. Formation of polyhedral shapes were accelerated for the reduced pressure.

2.2. Theoretical Results. Reduced pressure speeds up precipitation, leading to the frequent appearance of polyhedral particles. Then it raises the question of how these nonspherical particles acquire their shape. To address this question, we employ the mathematical model described in Section 5.2 providing a key insight. Our analysis unveils a dynamic perspective consistent with the experimental setup. The model, featuring two unknowns (u and v), is defined by energy in eq 1 where u represents particle shape, while v signifies microphase separation within. The associated Euler−Lagrange system is given by eqs 3−6. Crucially, the ratio of relaxation parameters τ_u and τ_v, governing time-derivative rates and process speeds, is pivotal. We maintain τ_u at a fixed value of 1, concentrating solely on varying τ_v. This dynamical reasoning arises from the contrast in speed between particle formation and microphase separation. As τ_v increases, microphase separation lags behind particle formation, indicating the emergence of polyhedral shapes, consistent with the accelerated particle precipitation observed experimentally.

2.2.1. Diagram of Cubes, Spirals, Layered Particles and Onions. Before discussing the relation between polyhedral shapes and the parameter τ_v, it is instructive to present a general diagram of morphologies for a variety of settings as depicted in Figure 2. The parameters and IC of this figure are in Appendix A.

The parameter b_1 serves as an indicator of the relative hydrophilicity or hydrophobicity of each polymer. As per convention, in Figure 2, the blue polymer exhibits a higher affinity for the solvent compared to the green polymer. For negative values of b_1, we have appropriately adjusted the corresponding ICs in reverse. We have organized six subsets of morphologies based on the magnitude of the b_1 parameter, with each subset encompassing morphologies for both small and large values of τ_v that are suitable for the given system size.

We first discuss the symmetric case of $b_1 = 0$ (d1−d2). A small value of τ_v results in a layered particle (d2), which is expected because both segments of the copolymer have the same interaction with the solvent. To show the symmetry of the layered particle in (d2), we have calculated the external area of each component of the particle in contact with the solvent to show that in fact both areas are identical, $A_{extB} = A_{extG}$, where A_{extB} is the external area of the particle with $v < 0$ (shown in blue) and A_{extG} is the external area of the particle with $v > 0$ (shown in green).

To maintain consistency across all different cases shown in this figure, all morphologies shown in this figure were constructed at the end of 10,000 time steps with the same IC. In most cases, the energy evolution suggests that a steady state has been reached. In particular for the layered particles shown in (d2) we verified the same morphology persists beyond 20,000 time steps.

At an early stage of the simulation of the layered particle we notice a plateau of energy with a transient cubic particle on it as in (d2). As the value of τ_v increases, the cubic particle persist and remain steady for over 10,000 time steps (d1) for the larger system size $L = 0.9$. It is not clear at this point that this cubic particle is a local minimizer or just a transient pattern by looking at the long-lasting plateau. In Section 2.2.3 it is shown

https://doi.org/10.1021/acsomega.3c10302
ACS Omega 2024, 9, 17276−17288

that this nonspherical morphology is robust against a numeric perturbation. In addition to the difference of τ_v, we use the appropriate system size for the layered and cubic particles. The choosing of the appropriate system size depends on the morphology and will be clarified in a subsequent section. For the moment it suffices to say that the system size is such that it promotes robustness of the corresponding particle against perturbations.

Now we discuss the nonsymmetric case of $b_1 = 0.04$ (e1−e2). A small value of τ_v results in a spiral particle (e2) whose segments no longer have equal interaction with the solvent and therefore the external areas of each component are different $A_{extB} \neq A_{extG}$. Similarly as in the previous case, as the value of τ_v increases, so does the lifetime of the cubic particle on the plateau, and thus for larger values of τ_v we obtain a steady cubic particle (e1). For $b_1 = 0.04$ we have selected the most appropriate value of the system size, which is different from the case of $b_1 = 0$. In Section 2.2.3 we study in detail the dependence of morphologies on the system size so as to clarify under which conditions the cubic particle maintains its shape.

The last case to discuss is the largest value of the interaction, $b_1 = 0.2$. Since this value of b_1 is quite big, we find onion morphologies for small and big values of τ_v, which is expected. The case of negative values of b_1 is also included on the left-hand side of Figure 2. Since the interaction is being reversed then the morphologies are all reversed versions of the cases discussed above. All morphologies shown in this figure are robust against a small perturbation.

It is important to make explicitly clear that the cubic morphology may be a transient one in general for a given τ_v and the system size, though it is possible to extend their lifespan by increasing the value of τ_v. In other words, there is an appropriate regime for the parameters τ_v and the system size in which they are realized as local minimizers. To distinguish between a local minimizer and a transient pattern is in general a quite subtle issue. We discuss more about this in subsequent sections.

A summary of the expected behavior of the external areas is shown at the center of the diagram. This diagram depicting the areas is intended solely for providing a qualitative explanation of the interaction between morphologies and the solvent. It is evident that the specific numeric values of the external areas are contingent upon the system's size. Nevertheless, it serves as an illustrative tool to discern that $A_{extB} \neq A_{extG}$ when $b_1 > 0$, while $A_{extB} = A_{extG}$ when $b_1 = 0$.

Here we remark about graphical representations of particles in this work—such as spirals, onions or cubes—consist of drawing the v component only. However, it is important to mention that the component u, at some given threshold, is a closed surface establishing a well-defined boundary around the nanoparticle and it decays quickly to -1 deserving of being called localized particles.

2.2.2. Plateau and Robustness of Cubic Morphologies. It is instructive to see the morphological changes as the ratio of speed factors is changed. Let us examine the case for the right middle class of Figure 2 with $b_1 = 0.04$. In Figure 3, as τ_v increases from (a) to (d), the final morphology is a particle resembling a layered ring morphology. It is noteworthy that intriguing morphologies for $\tau_v = 1$ are absent, as demonstrated in the Supporting Information.

As depicted in the Figure 3, larger values of τ_v lead to an extended period during which the cubic morphology remains almost unchanged, forming a plateau. This suggests that the role of τ_v is to postpone the transition from the cubic morphology to the layered ring morphology. Thus, it is reasonable to expect that if a large enough value of τ_v is chosen then the final morphology would be a cubic particle.

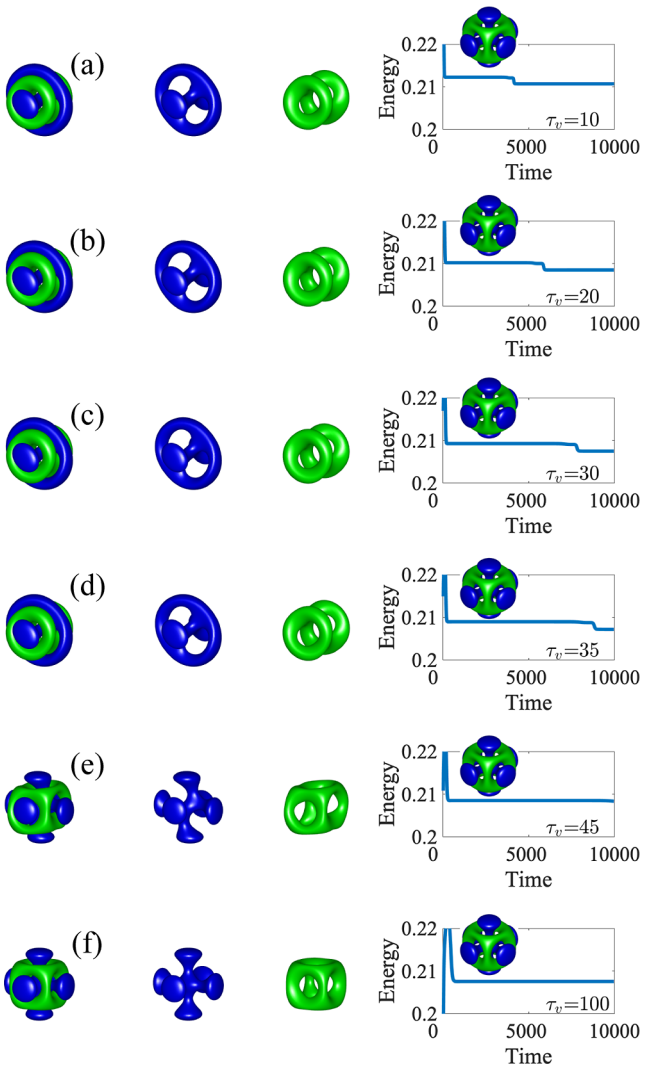

Figure 3. (a−f) Morphologies for increasing τ_v values. The cubic morphology sustains for an extended duration as τ_v is increased. The bottom row (f) illustrates an extreme case where τ_v must surpass a large value to maintain morphology for over 10,000 time steps. Note that morphology (e) slightly differs from morphology (f), yet both persist beyond 10,000 time steps. It turns out that (f) is a local minimizer, but (e) is transient pattern. See the text for details. Each snapshot on the plateaux corresponds to 3000 time steps. Parameters: $\sigma = 310$, $\epsilon_u = 0.02$, $\epsilon_v = 0.04$, $\tau_u = 1$, $b_1 = 0.04$, $b_2 = 1.0$, $L = 0.93$.

The bottom two cases of Figure 3e,f show that this could be in fact true. Using $\tau_v = 100$ results in a morphology with a quite long plateau and the energy appears to reach a steady level. Nevertheless, it is crucial to note that an extended plateau of (e) for $\tau_v = 45$ does not necessarily indicate its status as a local minimizer, resilient against numerical perturbations. In other words, it might represent a transient phase (possibly very close to a saddle point), albeit with weak instability. A meticulous examination of the profiles in Figure 3e reveals slight discrepancies from those in (f) when $\tau_v = 100$. As will be shown in the next section, the cubic morphology (f) for $\tau_v = 100$ turns out to be a local minimizer. This disparity implies that the plateau morphology observed at $\tau_v = 45$ is indeed a

https://doi.org/10.1021/acsomega.3c10302
ACS Omega 2024, 9, 17276−17288

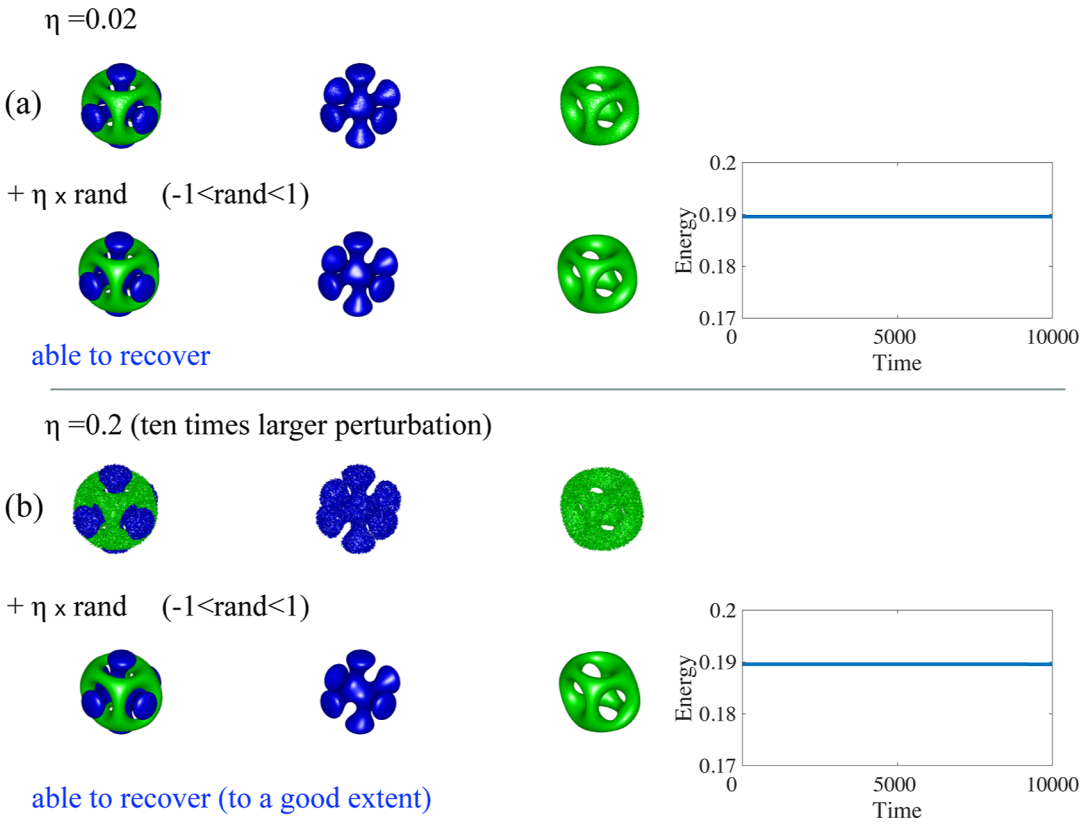

Figure 4. Cubic morphology stability at $L = 0.9$, $b_1 = 0$, and $\tau_v = 100$. Parameters: $\epsilon_u = 0.02$, $\epsilon_v = 0.04$, $\sigma = 310$. A perturbation of magnitude η is introduced to a cubic morphology, recovering the original shape for $\eta = 0.02$ (a) and $\eta = 0.2$ (b). The "rand" variable represents a random number in the interval $[-1, 1]$. The energy plotted on the right side remains nearly constant after the perturbation suggesting the stability of the cubic morphology.

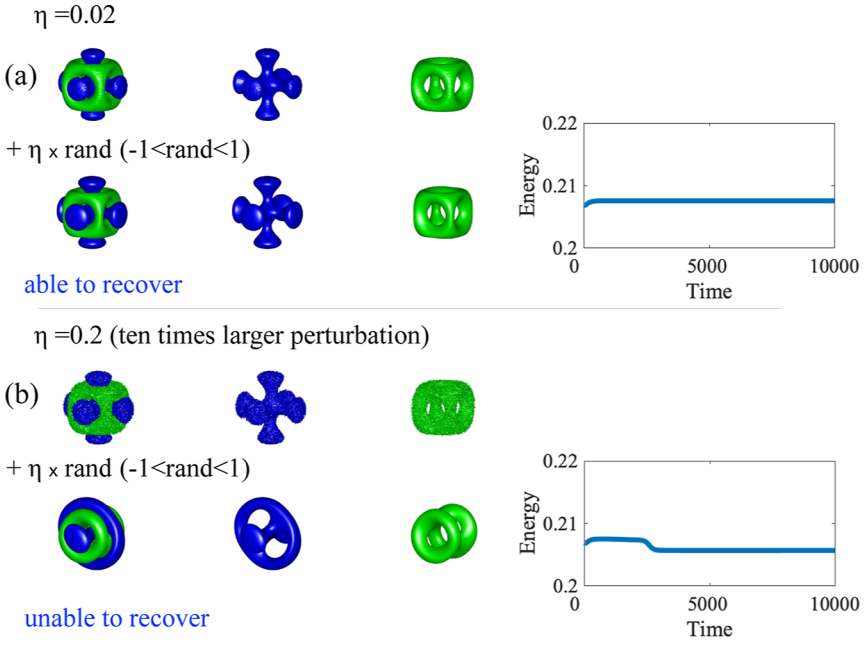

Figure 5. Cubic morphology stability at $L = 0.93$, $b_1 = 0.04$, and $\tau_v = 100$. Parameters: $\epsilon_u = 0.02$, $\epsilon_v = 0.04$, $\sigma = 310$. A perturbation of magnitude η is introduced to a cubic morphology, resulting in recovery only for the smaller perturbation $\eta = 0.02$ (a). The "rand" variable represents a random number in the interval $[-1, 1]$. For a larger perturbation $\eta = 0.2$ (b), the cubic structure transforms into a layered ring pattern resembling morphologies in Figure 3a–d.

transient state, and a transition between basins has taken place between $\tau_v = 45$ and $\tau_v = 100$. Another important consideration involves the careful selection of the system size to ensure robustness. We determined the best value for L by introducing perturbations to the final morphology at 10,000 time units. This involved systematically decreasing the value of

https://doi.org/10.1021/acsomega.3c10302
ACS Omega 2024, 9, 17276−17288

L from an initial L = 1.0. The objective was to identify the system size that maintains the cubic morphology for the longest interval of time at τ_v = 100. Through this process, it was verified that the most suitable value is L = 0.93, as substantiated by the subsequent stability assessment in the next section.

2.2.3. Stability of Morphologies. To test the stability of the 3D morphologies of Figures 2 and 3, we introduced small random uniform perturbations η with mean zero to order parameters u and v. These perturbed ICs were used to solve the CCH equations. The cubic-like particle in the top right of Figure 2d1 proved quite robust with L = 0.9 as shown in Figure 4. However, when simulated in a slightly larger system size (L = 1.0), it transformed into a different morphology (not shown here). We also confirmed the robustness of the layered and spiral particles in Figure 2d2,e2 with L = 0.8 (not shown here).

In Figure 5, we perturbed a cubic particle Figure 3f with L = 0.93, which is exactly the same as Figure 2e1, revealing its ability to withstand minor perturbations. For larger perturbations, the orbit crosses the border of basin of cubic and is attracted to a layered ring pattern.

Note that the configuration of Figure 3e is slightly different from (f) and not robust against small perturbation, therefore it occurs a basin switch from ring to cubic at some value of τ_v between 45 and 100.

Overall, these observations highlight the intricate and rugged nature of the free energy landscape. Nevertheless, by using an appropriate system size, we successfully reproduced polyhedral morphologies of cubic type for large values of τ_v. Remarkably, the structure of the landscape of free energy remains the same; however, the orbit dynamically changes the route as τ_v is increased, which corresponds to the change in experimental settings, such as a decrease in pressure.

2.2.4. Variation of Cubic Morphologies. Figure 6 presents several illustrative examples of particles exhibiting cubic or cubic-like morphologies. One intriguing aspect is the versatility in creating a wide spectrum of cubic shapes by manipulating the parameters detailed in eqs 3−6. This figure shows that, despite employing identical ICs, the resulting cubic particles exhibit notable structural variations depending on the parameters. The purpose of this figure is to display a variety of cubic-like particles for a broad range of σ = 360, 290, and 250 from top to bottom. The parameter σ is described Section 5.2. It is important to observe in this figure that the ϵ_v values differ: ϵ_v = 0.02 for (a), ϵ_v = 0.04 for (b), and ϵ_v = 0.02 for (c). Notice that, for instance, in the case depicted in Figure 6b, the green-colored component, representing $v > 0$ displays the presence of six voids, while the same component in case (c) lacks such voids. This observation suggests that cubic-like morphologies is ubiquitous, particularly when τ_v assumes significant values, albeit with distinct characteristics depending on the specific parameters. In essence, this flexibility enables the deliberate design of intricate internal structures within cubic morphologies, expanding the scope for detailed structural engineering within this cubic class of nanoparticle morphology.

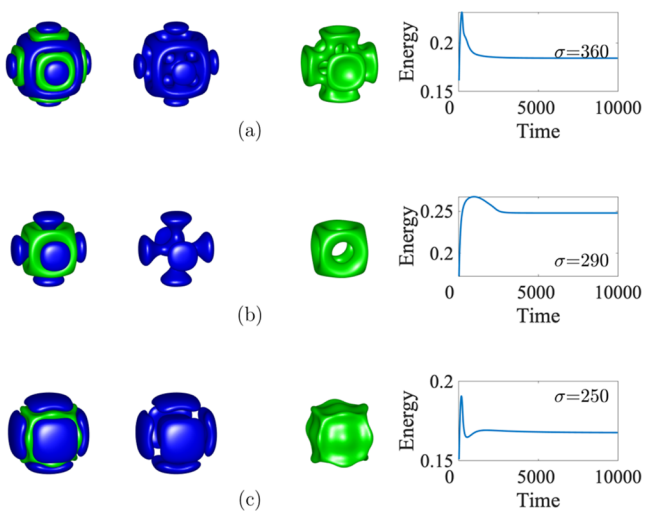

Figure 6. Variations of cubic morphologies. From top to bottom: (a) ϵ_v = 0.02 and σ = 360. (b) ϵ_v = 0.04 and σ = 290. (c) ϵ_v = 0.02 and σ = 250. All three cases above were initialized using the same ICs and τ_u = 1, τ_v = 400, ϵ_u = 0.02, b_1 = 0.04, b_2 = 1.0, L = 1.0.

3. DISCUSSION

The traditional exploration of particles in 3D confinement has predominantly centered on spherical particles, with investigations primarily focused on understanding the changes in their internal structures, as illustrated in Figure 1. However, the systems under scrutiny in our study reveal a departure from this conventional paradigm, where the polyhedral nanoparticles spontaneously emerge under an appropriate experimental condition. This intriguing observation constitutes a novel aspect of 3D confinement, one that has not been previously reported. Figure 7a presents a comprehensive view of the molecular weights and D/L_0 values associated with BCPs characterized by the typical 3D structures that have been extensively studied in prior research (refer to refs 8, 74 and 75). In this context, the red squares represent particles subjected to 3D confinement, featuring high molecular weights and D/L_0 values ranging from approximately 1.0 to 2.0. Notably, these conditions predominantly lead to the formation of lamellar phases, including uniaxially stacked lamellae and onion structures, resembling those observed in bulk systems. In stark contrast, our investigation focuses on a different region of parameter space, symbolized by the orange diamonds in Figure 7a. The BCP nanoparticles in this region possess molecular weights and D/L_0 values that significantly diverge from the previously reported 3D confinement systems. Specifically, the D/L_0 values in this regime range from approximately 3.0 to 4.5, a range that is conducive to the formation of intricate polyhedral morphologies. These contrasting characteristics between the two types of structures underscore the presence of additional influencing parameters beyond molecular weight and D/L_0 that shape the resulting particle structures. Another point of concern is the alignment between the theoretical model and the experimental system concerning the ratio D/L_0, which warrants additional elucidation. While acknowledging the validity of this point, it is crucial to note a computational limitation that hinders an extensive exploration of system sizes in three dimensions. Despite this constraint, there exists partial agreement between the theoretical model results and experimental findings. Notably, the sequence of diamonds along the vertical red line in Figure 7a corresponds to the polyhedra depicted in Figure 1C as D/L_0 increases. This correspondence can be reproducible to some extent numerically, as exemplified in Figure 7b−d within a suitable context. This observation poses a challenge for future investigations.

https://doi.org/10.1021/acsomega.3c10302
ACS Omega 2024, 9, 17276−17288

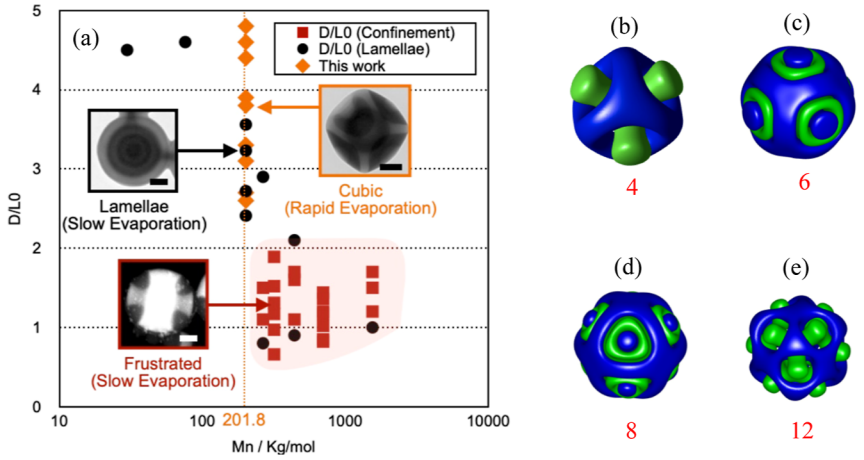

Figure 7. (a) Plot of D/L_0 and Mn values for phase-separated BCP particles, incorporating literature data (black dots and red squares) and results from this study (orange diamonds). The red-shaded region highlights particles forming 3D confinement structures. The scale bars in (a) represent 100 nm. (b−e) Examples of polyhedral particles obtained using the theoretical model proposed in this study. The particles, from (b) to (e), exhibit 4, 6, 8, and 12 faces, respectively. While the precise morphology depends on various parameters, generally, the number of faces increases with the width of the interface of the v component. The values of ϵ_v for these particles are 0.02, 0.02, 0.0208, and 0.036. The speed factors for the first and second particles are $\tau_v = 10$ and $\tau_v = 400$, while for the third and fourth cases, $\tau_v = 100$. In all instances, $\tau_u = 1$. In case (b), the value of σ is 310, while for the remaining cases, σ is set to 370. The system size is $L = 0.8$ for the first case, and $L = 1.0$ for the rest.

One notable departure between our current study and the previous work lies in the difference in pressure conditions. In the present study, particle formation occurred under reduced pressure conditions. This reduction in pressure has a substantial impact on the evaporation dynamics of the solvent, resulting in a more rapid deposition of particles. As evidenced in Figure 7a, two distinct TEM images depict slow and fast evaporation conditions. Remarkably, both images align along the same vertical axis, representing the molecular weight (Mn/kg/mol), with the only difference being the evaporation speed. Rapid evaporation under reduced pressure conditions notably leads to the formation of polyhedral nanoparticles. We establish a connection between this experimental parameter and the speed factor τ_v in one of the coupled Cahn−Hilliard equations. Numerical simulations affirm that cubic-like particles emerge and exhibit robustness against slight perturbations for large τ_v values and an appropriately chosen system size. These stable polyhedral nanoparticles persist even under small variations in both τ_v and system size. The swift precipitation of fine particles in reduced pressure environments is associated with a rapid decrease in polymer solubility, fostering the formation of fine particle seeds. Consequently, the ICs for particles in the early stages of formation differ substantially from those in slow particle formation scenarios conducted in a water bath at 40 °C. The role of concentration further supports these observations (see Appendix B). It is worth noting that a diverse range of cubic morphologies can be achieved through parameter adjustments, such as modifying σ, as detailed in Section 2.2.4. While our primary focus has centered on the cubical class of polyhedrons in this study, it is noteworthy that other types of Platonic polyhedra can be obtained within a different parameter regime, as demonstrated in Figure 7b−e. Crucially, the prerequisite for achieving polyhedral shapes remains the imposition of large τ_v values with τ_u being fixed to be 1. This opens a promising avenue for designing a diverse array of polyhedral nanoparticles by modulating the precipitation speed, in addition to considering the polymer species. The rugged landscape of the free energy function described in eq 1 of Section 5.2 presents a formidable challenge when attempting systematic searches for specific shapes. Conventional random search methodologies prove inadequate in this context, necessitating the development of novel guiding principles. Our work has embraced a unique dynamic regime, characterized by the acceleration of precipitation through the selection of large τ_v values, diverging from the conventional steepest descent approach ($\tau_v = 1.0$, see also Supporting Information). In conclusion, our study has unveiled a hitherto unexplored facet of nanoparticle formation within 3D confinement, where microphase-separated structures play a pivotal role in shaping particle morphology. The interplay of pressure, evaporation dynamics, and parameter selection, notably the speed factor τ_v, introduces an exciting dimension to our understanding of nanoparticle formation. This work not only expands the horizons of particle design but also underscores the intricate nature of free energy landscapes in guiding complex shape evolution. The elucidation of the underlying mathematical structure remains a significant challenge and a fertile ground for future research endeavors.

4. CONCLUSIONS

In conclusion, our study sheds light on the intricate challenges inherent in shaping experimental environments to achieve desired outcomes in scientific endeavors, particularly when dynamic processes are at play. Through the utilization of the CCH model, we have provided a tangible example of how precise control over experimental conditions can lead to the creation of polyhedral nanoparticles.

A key finding of our research centers on the morphology induced by formation speed, specifically, how a reduction in pressure intensifies the precipitation rate. This, in turn, leads to the efficient production of PBCP particles, vividly exemplified in Figure 1. This acceleration is achieved by carefully manipulating the ratio of the relaxation parameters, τ_u and τ_v, within the CCH model. The impact of concentration, as elaborated in Appendix B, further bolsters our findings.

Our work highlights the unique challenges posed by dynamic processes and the fundamental role played by the CCH model in shaping outcomes. Notably, the emergence of

https://doi.org/10.1021/acsomega.3c10302
ACS Omega 2024, 9, 17276−17288

polyhedral morphologies is intricately linked to the ratio of relaxation parameters, and conventional steepest descent approaches prove inadequate in capturing this phenomenon. This suggests that the solution trajectory is not orthogonal to the contour lines but rather inclined, underscoring the critical role of dynamic processes.

Importantly, we do not alter any parameters of the free energy; thus, the experimental outcome is solely dictated by the dynamical processes. This implies the significance of dynamic processes in shaping experimental results, emphasizing that a thorough understanding of the free energy landscape alone is insufficient for prediction, as it does not elucidate how the solution trajectory navigates this landscape. This aspect also poses a formidable mathematical challenge for future research endeavors.

Moreover, we emphasize that the influence of pressure on the formation of polyhedral particles is independent of chemical species or molecular weights. Elevating τ_v has been identified as a crucial factor to produce polyhedral particles in our CCH mode. Additionally, our calculations underscore the pivotal role of selecting an appropriate system size L in generating a diverse array of transient and local minimizers (See the Subsection 2.2.3 and the diagram in Supporting Information).

In sum, our research not only offers practical insights into controlling the formation of polyhedral nanoparticles but also highlights the intricate interplay of dynamic processes, relaxation parameters, and environmental factors. This work contributes to the broader understanding of experimental design and provides valuable guidance for future studies in materials science and nanotechnology.

5. METHODS

5.1. Materials. Polystyrene-*block*-polyisoprene (PS-*b*-PI, Mn_{PS} = 201.8 kg/mol, Mn_{PI} = 210 kg/mol, ϕ_{PI} = 0.54, Mw/Mn = 1.13) was purchased from Polymer Source, Inc. (Quebeck, Canada). Tetrahydrofran (THF/GR) and aqueous solution of osmium tetraoxide (OsO_4) 0.2 wt % were purchased from Fujifilm Wako Chemical Industry, Inc. (Osaka, Japan).

5.1.1. Preparation of Diblock Copolymer Particles. PS-*b*-PI was dissolved in THF to prepare 0.1−5.0 mg/mL solution. 1.0 mL of membrane-filtered water was mixed into the solution in a glass bottle at its mixing speed of 1.0 mL/min with stirring. After stopping the stirring, THF was evaporated at 40 °C water bath or in vacuo at room temperature using a Smart Evaporator K4, BioChromato, Inc. (Fujisawa, Japan). After complete evaporation of THF, aqueous dispersions of PS-*b*-PI particles were obtained. The size distribution of particles was measured by DLS (ZS-1, Malvern, U.K.).

5.1.2. Observation of Nanostructures. PI phases were stained and cross-linked with OsO_4 by mixing 500 μL of 0.2 wt % OsO_4 aq. into the 1 mL of particle dispersion and standing for 2 h. The stained particles were corrected by centrifugation (12,000 rpm, 15 min, 5 °C) and washed with membrane-filtered water. Cu grids with an elastic carbon membrane were hydrophilized with UV−O3 treatment for 5 min. One drop of an aqueous dispersion of particles was dropped onto a grid surface and dried at room temperature. The particles on the Cu grid were observed by TEM (H-7650, Hitachi, Japan). The samples were observed by TEM with varying tilt angles from −60 to 60 with a step of 1 (120 images were obtained) (ref 71). The obtained images were stacked using the imaging software ImageJ (ver. 1.48v, NIH, United States), and then tilting axis alignment and reconstruction of *xy* sliced images were performed using a plug-in for ImageJ, TomoJ (freely provided by Centre Universitaire d'Orsay, France).[76] The generation of 3D reconstruction images and abstraction of the outlines were performed using HawkC, which was freely provided by Osaka University, Japan.[77] Cross-sectional images and reconstruction of the 3D images were generated using CINEMA 4D (MAXON Computer, GmbH, Germany).

5.2. Theoretical Model. The dynamics of the state of the two mixed systems under consideration, the two order variables u and v evolve to minimize the value of an energy functional in the following expression. Here u represents a shape of the particle and v for microphase separation inside the particle.

$$F \equiv F_{\epsilon_u,\epsilon_v,\sigma}(u, v) = \int_\Omega \left\{ \frac{\epsilon_u^2}{2}|\nabla u|^2 + \frac{\epsilon_v^2}{2}|\nabla v|^2 + W(u, v) + \frac{\sigma}{2}|(-\Delta)^{-1/2}(v - \bar{v})|^2 \right\} dr \quad (1)$$

where

$$W(u, v) = \frac{(u^2 - 1)^2}{4} + \frac{(v^2 - 1)^2}{4} + b_1 uv - b_2 \frac{uv^2}{2} \quad (2)$$

Loosely speaking, the constant-height surface $u = 0$ stands for the boundary of the particle, and $v = \pm 1$ shows A (or B)-polymer rich region, respectively, for the BCP A-*b*-B. In eq 1, Ω is a smooth bounded domain in IR^N. Here we focus on 3D confinement and thus $N = 3$. Parameters ϵ_u and ϵ_v control the size of the interface of u and v.

In this investigation, although the systematic exploration of σ's impact on polyhedral particles is not undertaken, it is crucial to acknowledge its significance. σ is associated with the bonding between block A and block B in the copolymer, exhibiting an inverse proportionality to the square of the BCP length (or molecular weight). Shorter BCP units result in larger σ, fostering stronger long-range interactions among particles. The parameter σ plays a pivotal role in Figure 7a, delineating the red-shaded region (representing prior studies) from the orange diamonds (representing the current study). The variable u minimizes the free energy by segregating the space into copolymer and solvent-rich domains, defining the shape of the particle. Conversely, v governs the microphase separation within the copolymer domain, leading to a variety of morphologies. Larger σ values often lead to more intricate particle shapes due to an increased number of interfaces in the spatial domain.

The associated Euler−Lagrange system of equations corresponding to the mixed system are the following

$$\tau_u u_t = \Delta\left(\frac{\delta F}{\delta u}\right) \quad (3)$$

$$= -\Delta\left\{\epsilon_u^2 \Delta u + (1 - u)(1 + u)u - b_1 v + \frac{b_2}{2}v^2\right\} \quad (4)$$

$$\tau_v v_t = \Delta\left(\frac{\delta F}{\delta v}\right) \quad (5)$$

https://doi.org/10.1021/acsomega.3c10302
ACS Omega 2024, 9, 17276−17288

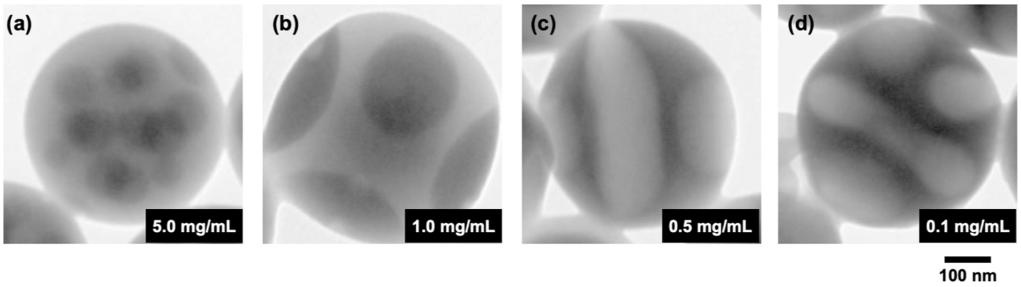

Figure 8. TEM images of PS-*b*-PI particles obtained from THF solutions of 5.0 mg/mL (a), 1.0 mg/mL(b), 0.5 mg/mL(c), and 0.1 mg/mL(d), respectively.

$$= -\Delta\{\epsilon_v^2 \Delta v + (1 - v)(1 + v)v - b_1 u + b_2 uv\} - \sigma(v - \overline{v}) \quad (6)$$

where the parameters τ_u and τ_v are time constants to control the speed at which parameters u and v evolve. Since τ_u and τ_v are dimensional parameters, the value of $\tau_u = 1$ is fixed throughout this work to avoid any confusion. For the majority of the calculations we used an onion-like morphology as IC consisting on a spherical core with $v < 0$, a shell with $v > 0$, and $v = 0$ outside the particle. The radius of the core and the thickness of the shell are approximately of the same length. We use a 3D cubic domain of length L and periodic boundary conditions to solve the CCH equations.

To integrate eqs 4 and 6, we employ a modified version of the linear implicit scheme discussed in refs 78 and 79, addressing nonlinearity by dividing the cubic term into a quadratic term for the system's state at the initial time-step and a linear term for the subsequent time-step. This modification ensures numerical stability with larger time steps (e.g., $\Delta t \approx 0.01$) but requires caution. While the energy remains bounded, achieving a monotonous decrease is challenging. We suspect that nonlinear terms in the energy expression related to the double-well potential contribute to energy growth. Nonetheless, a spectral scheme confirms that cubic morphologies persist with the same ICs and parameters. The numerical solution of these coupled equations yields morphologies of minimum free energy with sufficient simulation time. Additionally, solving the CCH equations maintains constant total volume, where v_0 represents the initial distribution of BCP across the domain. Our model employs a 128 × 128 × 128 cubic lattice with periodic boundary conditions along X, Y, and Z axes to simulate morphologies similar to experimental observations. The system size L is related to the number of grid points, N. For example, in the X axis, $N = 128$ and $L = N\Delta x$ (similarly for Y and Z), where Δx is the mesh size, which determines the spacing between nodes in the X axis. Similarly Δy, and Δz in the y, and z axes, respectively. 3D morphologies are visualized using isosurfaces at suitable values of the order parameter v.

APPENDIX A

Scheme of morphologies

The parameters employed in Figure 2 are the following. The parameters common to all cases are $\sigma = 310$, $\epsilon_u = 0.02$, $\epsilon_v = 0.04$, $\overline{u} = -0.50$, $\overline{v} = 0.0$. $\tau_u = 1$, $b_2 = 1.0$. Total simulation time is 10,000 time steps. The IC is an onion-like morphology as described in Section 5.2.

The parameters for each particular case: (a1) Cube with $\tau_v = 100$ ($L = 0.9$). (a2) Layered particle with $\tau_v = 10$ ($L = 0.78$). (a3) Transient cube at early time in (a2), ($L = 0.78$). Common parameters: $b_1 = 0.0$. (IC reversed).

(b1) Cube with $\tau_v = 100$ ($L = 0.93$). (b2) Spiral with $\tau_v = 10$ ($L = 0.8$). (b3) Transient cube at early time of (b2), ($L = 0.8$). Each plateau of energy has a cubic morphology. When τ_v becomes large the spiral is delayed and eventually it vanishes for sufficiently large τ_v. Common parameters: $b_1 = -0.04$. (IC reversed).

(c1) $L = 1.0$, (c2) $L = 0.8$. When b_1 is large we get onions, as expected. Common parameters: $b_1 = -0.2$, (IC reversed).

(d1) Cube with $\tau_v = 100$ ($L = 0.9$). (d2) Layered particle with $\tau_v = 10$ ($L = 0.78$). (d3) Transient cube at early time in (a2), ($L = 0.78$). Common parameters: common parameters: $b_1 = 0.0$. (IC original).

(e1) Cube with $\tau_v = 100$ ($L = 0.93$). (e2) Spiral with $\tau_v = 10$ ($L = 0.8$). (e3) Transient cube at early time of (b2), ($L = 0.8$). Common parameters: $b_1 = 0.04$. (IC Original).

(f1) $L = 1.0$, (f2) $L = 0.8$. When b_1 is large we get onions, as expected. Common parameters: $b_1 = 0.2$. (IC original).

APPENDIX B

Effect of concentration

An additional critical parameter influencing the deposition rate of particles under experimental conditions is the initial concentration of the polymer solution. In the sequential osmotic-reduction precipitation method employed in our study, particle formation occurs during the precipitation of the polymer from the polymer solution into the aqueous phase. Consequently, for a constant molecular weight and consistent solubility, it is observed that higher concentrations lead to a more rapid precipitation process.

To illustrate the significant role of concentration in shaping particle morphology, Figure 8 depicts the structural characteristics of nanoparticles of identical size (with a D/L_0 ratio of 3.6) at varying solution concentrations.

At lower concentration values, such as 0.5 and 0.1 mg/mL, as shown in (c,d) respectively, a lamellar-like phase is formed, with the PI phase predominantly occupying the particle surface.

In contrast, when the concentration is increased to 1.0 mg/mL, cubic-like particles are observed, as depicted in (b). However, when the concentration is raised to a significantly higher level, exemplified by the particle produced from a 5.0 mg/mL solution, as seen in (a), a complex morphology emerges. This particle exhibits a PS (polystyrene) phase on its surface and a dot-like PI (polyisoprene) phase in its interior, despite possessing a similar size to the previously mentioned particles. This observation suggests that the two fundamental processes, namely particle shape formation and microphase

https://doi.org/10.1021/acsomega.3c10302
ACS Omega 2024, 9, 17276−17288

separation, do not evolve in a synchronized manner, leading to the production of polyhedral shapes.

In summary, the concentration of the initial polymer solution exerts a profound influence on the resulting particle structure. Our observations demonstrate that subtle variations in concentration can lead to dramatically different morphologies, highlighting the intricate interplay between concentration, microphase separation, and particle formation. This phenomenon underscores the complexity of nanoparticle design in confined environments and presents exciting opportunities for further exploration and control of particle morphology in such systems.

■ ASSOCIATED CONTENT

Supporting Information

The Supporting Information is available free of charge at https://pubs.acs.org/doi/10.1021/acsomega.3c10302.

Details of a phase diagram of morphologies with b_1 = 0.04 (PDF)

■ AUTHOR INFORMATION

Corresponding Authors

Edgar Avalos − *Advanced Institute for Materials Research (WPI-AIMR), Tohoku University, Sendai, Miyagi 980-8577, Japan*; orcid.org/0000-0002-3009-6176; Email: soyedgaravalos@gmail.com

Hiroshi Yabu − *Advanced Institute for Materials Research (WPI-AIMR), Tohoku University, Sendai, Miyagi 980-8577, Japan*; orcid.org/0000-0002-1943-6790; Email: hiroshi.yabu.d5@tohoku.ac.jp

Yasumasa Nishiura − *Research Center of Mathematics for Social Creativity, Research Institute for Electronic Science, Hokkaido University, Sapporo 060-0812, Japan; Advanced Institute for Materials Research (WPI-AIMR), Tohoku University, Sendai, Miyagi 980-8577, Japan*; Email: nishiura@tohoku.ac.jp

Authors

Takashi Teramoto − *Faculty of Data Science, Kyoto Women's University, Kyoto 605-8501, Japan*

Yutaro Hirai − *Advanced Institute for Materials Research (WPI-AIMR), Tohoku University, Sendai, Miyagi 980-8577, Japan;* Present Address: AZUL Energy, Inc., 1-9-1, Ichibancho, Aoba-Ku, Sendai 980-0811, Japan

Complete contact information is available at: https://pubs.acs.org/10.1021/acsomega.3c10302

Notes

The authors declare no competing financial interest.

■ ACKNOWLEDGMENTS

H.Y. and Y.H. thank Minori Suzuki, WPI-AIMR, Tohoku University, for helping with TEM and ET imaging. This research was partially supported by KAKENHI (nos. 19KK0357, 20K20341, 20H04625, 23K03209, and 23K17653), MEXT, Japan. Thanks are extended to the anonymous reviewers for their insightful comments and valuable contributions.

■ REFERENCES

(1) Fasolka, M. J.; Mayes, A. M. Block Copolymer Thin Films: Physics and Applications. *Annu. Rev. Mater. Res.* **2001**, *31*, 323−355.

(2) Knoll, A.; Horvat, A.; Lyakhova, K. S.; Krausch, G.; Sevink, G. J. A.; Zvelindovsky, A. V.; Magerle, R. Phase Behavior in Thin Films of Cylinder-Forming Block Copolymers. *Phys. Rev. Lett.* **2002**, *89*, 035501.

(3) Zettl, U.; Knoll, A.; Tsarkova, L. Effect of Confinement on the Mesoscale and Macroscopic Swelling of Thin Block Copolymer Films. *Langmuir* **2010**, *26*, 6610−6617.

(4) Albert, J. N.; Epps, T. H. Self-assembly of block copolymer thin films. *Mater. Today* **2010**, *13*, 24−33.

(5) Li, W.; Liu, M.; Qiu, F.; Shi, A.-C. Phase Diagram of Diblock Copolymers Confined in Thin Films. *J. Phys. Chem. B* **2013**, *117*, 5280−5288.

(6) Jang, J. D.; Seo, H.-J.; Yoon, Y.-J.; Choi, S.-H.; Han, Y. S.; Kim, T.-H. Conformational control of two-dimensional gold nanoparticle arrays in a confined geometry within a vesicular wall. *Sci. Rep.* **2022**, *12*, 4548.

(7) Dobriyal, P.; Xiang, H.; Kazuyuki, M.; Chen, J.-T.; Jinnai, H.; Russell, T. P. Cylindrically Confined Diblock Copolymers. *Macromolecules* **2009**, *42*, 9082−9088.

(8) Higuchi, T.; Tajima, A.; Motoyoshi, K.; Yabu, H.; Shimomura, M. Frustrated Phases of Block Copolymers in Nanoparticles. *Angew. Chem., Int. Ed.* **2008**, *47*, 8044−8046.

(9) Rider, D. A.; Chen, J. I. L.; Eloi, J.-C.; Arsenault, A. C.; Russell, T. P.; Ozin, G. A.; Manners, I. Controlling the Morphologies of Organometallic Block Copolymers in the 3-Dimensional Spatial Confinement of Colloidal and Inverse Colloidal Crystals. *Macromolecules* **2008**, *41*, 2250−2259.

(10) Deng, R.; Liu, S.; Li, J.; Liao, Y.; Tao, J.; Zhu, J. Mesoporous Block Copolymer Nanoparticles with Tailored Structures by Hydrogen-Bonding-Assisted Self-Assembly. *Adv. Mater.* **2012**, *24*, 1889−1893.

(11) Yabu, H.; Higuchi, T.; Jinnai, H. Frustrated phases: polymeric self-assemblies in a 3D confinement. *Soft Matter* **2014**, *10*, 2919−2931.

(12) Yan, N.; Zhu, Y.; Jiang, W. Recent progress in the self-assembly of block copolymers confined in emulsion droplets. *Chem. Commun.* **2018**, *54*, 13183−13195.

(13) Yan, N.; Song, Y.; Zhu, Y. Confined self-assembly of block copolymers in emulsion droplets: Preparation, shape and internal structure, and applications. *J. Polym. Sci.* **2023**, *61*, 3211−3227.

(14) Dai, X.; Qiang, X.; Hils, C.; Schmalz, H.; Gröschel, A. H. Frustrated Microparticle Morphologies of a Semicrystalline Triblock Terpolymer in 3D Soft Confinement. *ACS Nano* **2021**, *15*, 1111−1120.

(15) Shin, K.; Xiang, H.; Moon, S. I.; Kim, T.; McCarthy, T. J.; Russell, T. P. Curving and Frustrating Flatland. *Science* **2004**, *306*, 76.

(16) Sun, Y.; Steinhart, M.; Zschech, D.; Adhikari, R.; Michler, G. H.; Gosele, U. Diameter-Dependence of the Morphology of PS-b-PMMA Nanorods Confined Within Ordered Porous Alumina Templates. *Macromol. Rapid Commun.* **2005**, *26*, 369−375.

(17) Xiang, H.; Shin, K.; Kim, T.; Moon, S. I.; McCarthy, T. J.; Russell, T. P. Block Copolymers under Cylindrical Confinement. *Macromolecules* **2004**, *37*, 5660−5664.

(18) Xiang, H.; Shin, K.; Kim, T.; Moon, S.; McCarthy, T. J.; Russell, T. P. The influence of confinement and curvature on the morphology of block copolymers. *J. Polym. Sci., Part B: Polym. Phys.* **2005**, *43*, 3377−3383.

(19) Xiang, H.; Shin, K.; Kim, T.; Moon, S. I.; McCarthy, T. J.; Russell, T. P. From Cylinders to Helices upon Confinement. *Macromolecules* **2005**, *38*, 1055−1056.

(20) Li, W.; Wickham, R. A.; Garbary, R. A. Phase Diagram for a Diblock Copolymer Melt under Cylindrical Confinement. *Macromolecules* **2006**, *39*, 806−811.

(21) Li, W.; Wickham, R. A. Self-Assembled Morphologies of a Diblock Copolymer Melt Confined in a Cylindrical Nanopore. *Macromolecules* **2006**, *39*, 8492−8498.

(22) Li, W.; Wickham, R. A. Influence of the Surface Field on the Self-Assembly of a Diblock Copolymer Melt Confined in a Cylindrical Nanopore. *Macromolecules* **2009**, *42*, 7530−7536.

(23) He, X.; Liang, H.; Song, M.; Pan, C. Possibility of design of nanodevices by confined macromolecular self-assembly. *Macromol. Theory Simul.* **2002**, *11*, 379−382.
(24) Feng, J.; Liu, H.; Hu, Y. Mesophase Separation of Diblock Copolymer Confined in a Cylindrical Tube Studied by Dissipative Particle Dynamics. *Macromol. Theory Simul.* **2006**, *15*, 674−685.
(25) Feng, J.; Ruckenstein, E. Morphologies of AB Diblock Copolymer Melts Confined in Nanocylindrical Tubes. *Macromolecules* **2006**, *39*, 4899−4906.
(26) Xu, J.-B.; Wu, H.; Lu, D.-Y.; He, X.-F.; Zhao, Y.-H.; Wen, H. Dissipative particle dynamics simulation on the meso-scale structure of diblock copolymer under cylindrical confinement. *Mol. Simul.* **2006**, *32*, 357−362.
(27) Chen, P.; Liang, H.; Shi, A.-C. Origin of Microstructures from Confined Asymmetric Diblock Copolymers. *Macromolecules* **2007**, *40*, 7329−7335.
(28) Feng, J.; Ruckenstein, E. Self-assembling of ABC linear triblock copolymers in nanocylindrical tubes. *J. Chem. Phys.* **2007**, *126*, 124902.
(29) Wang, Q. Symmetric diblock copolymers in nanopores: Monte Carlo simulations and strong-stretching theory. *J. Chem. Phys.* **2007**, *126*, 024903.
(30) Xiao, X.; Huang, Y.; Liu, H.; Hu, Y. Monte Carlo Simulation of ABA Triblock Copolymer Melts Confined in a Cylindrical Nanotube. *Macromol. Theory Simul.* **2007**, *16*, 166−177.
(31) Zhu, Y.; Jiang, W. Self-Assembly of Diblock Copolymer Mixtures in Confined States: A Monte Carlo Study. *Macromolecules* **2007**, *40*, 2872−2881.
(32) Chen, P.; Liang, H. Cylinder-Forming Triblock Terpolymer in Nanopores: A Monte Carlo Simulation Study. *J. Phys. Chem. B* **2008**, *112*, 1918−1925. PMID: 18217740
(33) Xiao, X.; Huang, Y.; Liu, H.; Hu, Y. Morphology Transition of Block Copolymers under Curved Confinement. *Macromol. Theory Simul.* **2007**, *16*, 732−741.
(34) Zhang, T.; Deng, H.; Yang, T.; Li, W. Defective morphologies kinetically formed in diblock copolymers under the cylindrical confinement. *Polymer* **2015**, *65*, 168−174.
(35) Higuchi, T.; Tajima, A.; Motoyoshi, K.; Yabu, H.; Shimomura, M. Suprapolymer Structures from Nanostructured Polymer Particles. *Angew. Chem., Int. Ed.* **2009**, *48*, 5125−5128.
(36) Zhang, M.; Hou, Z.; Liu, S.; Han, G.; Tian, M.; Zhu, J.; Xu, J. Temperature/pH dual-responsive reversible morphology evolution of block copolymer microparticles under three-dimensional confinement. *Sci. China: Chem.* **2023**, *66*, 3587−3593.
(37) Chen, C.; Wylie, R. A. L.; Klinger, D.; Connal, L. A. Shape Control of Soft Nanoparticles and Their Assemblies. *Chem. Mater.* **2017**, *29*, 1918−1945.
(38) Yabu, H.; Higuchi, T.; Shimomura, M. Unique Phase-Separation Structures of Block-Copolymer Nanoparticles. *Adv. Mater.* **2005**, *17*, 2062−2065.
(39) Higuchi, T.; Tajima, A.; Yabu, H.; Shimomura, M. Spontaneous formation of polymer nanoparticles with inner micro-phase separation structures. *Soft Matter* **2008**, *4*, 1302−1305.
(40) Hirai, Y.; Wakiya, T.; Yabu, H. Virus-like particles composed of sphere-forming polystyrene-block-poly(t-butyl acrylate) (PS-b-PtBA) and control of surface morphology by homopolymer blending. *Polym. Chem.* **2017**, *8*, 1754−1759.
(41) Kang, Y.; Cretu, O.; Kikkawa, J.; Kimoto, K.; Nara, H.; Nugraha, A. S.; Kawamoto, H.; Eguchi, M.; Liao, T.; Sun, Z.; Asahi, T.; Yamauchi, Y. Mesoporous multimetallic nanospheres with exposed highly entropic alloy sites. *Nat. Commun.* **2023**, *14*, 4182.
(42) Steinhaus, A.; Pelras, T.; Chakroun, R.; Gröschel, A. H.; Müllner, M. Confinement Assembly: Self-Assembly of Diblock Molecular Polymer Brushes in the Spherical Confinement of Nanoemulsion Droplets. *Macromol. Rapid Commun.* **2018**, *39*, 1800177.
(43) Azhdari, S.; Herrmann, F.; Coban, D.; Linders, J.; Gröschel, A. H. Confinement Assembly of Terpolymer-Based Janus Nanoparticles. *Macromol. Rapid Commun.* **2022**, *43*, 2100932.
(44) Kim, E. J.; Shin, J. J.; Do, T.; Lee, G. S.; Park, J.; Thapar, V.; Choi, J.; Bang, J.; Yi, G.-R.; Hur, S.-M.; Kim, J. G.; Kim, B. J. Molecular Weight Dependent Morphological Transitions of Bottlebrush Block Copolymer Particles: Experiments and Simulations. *ACS Nano* **2021**, *15*, 5513−5522.
(45) Higuchi, T.; Motoyoshi, K.; Sugimori, H.; Jinnai, H.; Yabu, H.; Shimomura, M. Phase Transition and Phase Transformation in Block Copolymer Nanoparticles. *Macromol. Rapid Commun.* **2010**, *31*, 1773−1778.
(46) Higuchi, T.; Shimomura, M.; Yabu, H. Reorientation of Microphase-Separated Structures in Water-Suspended Block Copolymer Nanoparticles through Microwave Annealing. *Macromolecules* **2013**, *46*, 4064−4068.
(47) Hu, D.; Chang, X.; Xu, Y.; Yu, Q.; Zhu, Y. Light-Enabled Reversible Shape Transformation of Block Copolymer Particles. *ACS Macro Lett.* **2021**, *10*, 914−920.
(48) Shin, J. M.; Kim, Y.; Yun, H.; Yi, G.-R.; Kim, B. J. Morphological Evolution of Block Copolymer Particles: Effect of Solvent Evaporation Rate on Particle Shape and Morphology. *ACS Nano* **2017**, *11*, 2133−2142. PMID: 28165714
(49) Vernizzi, G.; Sknepnek, R.; Olvera de la Cruz, M. Platonic and Archimedean geometries in multicomponent elastic membranes. *Proc. Natl. Acad. Sci. U.S.A.* **2011**, *108*, 4292−4296.
(50) Bowick, M. J.; Sknepnek, R. Pathways to faceting of vesicles. *Soft Matter* **2013**, *9*, 8088.
(51) Su, J.; Yao, Z.; Olvera de la Cruz, M. Vesicle Geometries Enabled by Dynamically Trapped States. *ACS Nano* **2016**, *10*, 2287−2294.
(52) Wong, C. K.; Martin, A. D.; Floetenmeyer, M.; Parton, R. G.; Stenzel, M. H.; Thordarson, P. Faceted polymersomes: a sphere-to-polyhedron shape transformation. *Chem. Sci.* **2019**, *10*, 2725−2731.
(53) Wong, C. K.; Stenzel, M. H.; Thordarson, P. Non-spherical polymersomes: formation and characterization. *Chem. Soc. Rev.* **2019**, *48*, 4019−4035.
(54) Alexandridis, P.; Tsianou, M. Block copolymer-directed metal nanoparticle morphogenesis and organization. *Eur. Polym. J.* **2011**, *47*, 569−583.
(55) He, X.; Song, M.; Liang, H.; Pan, C. Self-assembly of the symmetric diblock copolymer in a confined state: Monte Carlo simulation. *J. Chem. Phys.* **2001**, *114*, 10510−10513.
(56) Feng, J.; Liu, H.; Hu, Y. Micro-phase separation of diblock copolymer in a nanosphere: Dissipative particle dynamics approach. *Fluid Phase Equilib.* **2007**, *261*, 50−57. Properties and Phase Equilibria for Product and Process Design 11th International Conference on Properties and Phase Equilibria for Product and Process Design
(57) Chen, P.; Liang, H.; Shi, A.-C. Microstructures of a Cylinder-Forming Diblock Copolymer under Spherical Confinement. *Macromolecules* **2008**, *41*, 8938−8943.
(58) Pinna, M.; Guo, X.; Zvelindovsky, A. V. Block copolymer nanoshells. *Polymer* **2008**, *49*, 2797−2800.
(59) Han, Y.; Cui, J.; Jiang, W. Effect of Polydispersity on the Self-Assembly Structure of Diblock Copolymers under Various Confined States: A Monte Carlo Study. *Macromolecules* **2008**, *41*, 6239−6245.
(60) Yu, B.; Li, B.; Jin, Q.; Ding, D.; Shi, A.-C. Self-Assembly of Symmetric Diblock Copolymers Confined in Spherical Nanopores. *Macromolecules* **2007**, *40*, 9133−9142.
(61) Yu, B.; Sun, P.; Chen, T.; Jin, Q.; Ding, D.; Li, B.; Shi, A.-C. Self-assembled morphologies of diblock copolymers confined in nanochannels: Effects of confinement geometry. *J. Chem. Phys.* **2007**, *126*, 204903.
(62) Yu, B.; Sun, P.; Chen, T.; Jin, Q.; Ding, D.; Li, B.; Shi, A.-C. Self-assembly of diblock copolymers confined in cylindrical nanopores. *J. Chem. Phys.* **2007**, *127*, 114906.
(63) Yu, B.; Li, B.; Jin, Q.; Ding, D.; Shi, A.-C. Confined self-assembly of cylinder-forming diblock copolymers: effects of confining geometries. *Soft Matter* **2011**, *7*, 10227−10240.

https://doi.org/10.1021/acsomega.3c10302
ACS Omega 2024, 9, 17276−17288

(64) Li, S.; Chen, P.; Zhang, L.; Liang, H. Geometric Frustration Phases of Diblock Copolymers in Nanoparticles. *Langmuir* **2011**, *27*, 5081−5089. PMID: 21417241
(65) Li, S.; Liu, M.; Ji, Y.; Zhang, L.; Liang, H. Surface-field-induced microstructures of asymmetric diblock copolymer nanoparticles. *Polym. J.* **2011**, *43*, 606−612.
(66) Yang, R.; Li, B.; Shi, A.-C. Phase Behavior of Binary Blends of Diblock Copolymer/Homopolymer Confined in Spherical Nanopores. *Langmuir* **2012**, *28*, 1569−1578. PMID: 22148840
(67) Li, S.; Jiang, Y.; Chen, J. Z. Y. Morphologies and phase diagrams of ABC star triblock copolymers confined in a spherical cavity. *Soft Matter* **2013**, *9*, 4843−4854.
(68) Zhang, L.; Lin, J. Theoretical and Simulation Studies of Hierarchical Nanostructures Self-Assembled from Soft Matter Systems. *Self-Assembling Syst.* **2016**, 254−287.
(69) Avalos, E.; Higuchi, T.; Teramoto, T.; Yabu, H.; Nishiura, Y. Frustrated phases under three-dimensional confinement simulated by a set of coupled Cahn-Hilliard equations. *Soft Matter* **2016**, *12*, 5905−5914.
(70) Avalos, E.; Teramoto, T.; Komiyama, H.; Yabu, H.; Nishiura, Y. Transformation of Block Copolymer Nanoparticles from Ellipsoids with Striped Lamellae into Onionlike Spheres and Dynamical Control via Coupled Cahn-Hilliard Equations. *ACS Omega* **2018**, *3*, 1304−1314.
(71) Hirai, Y.; Avalos, E.; Teramoto, T.; Nishiura, Y.; Yabu, H. Ashura Particles: Experimental and Theoretical Approaches for Creating Phase-Separated Structures of Ternary Blended Polymers in Three-Dimensionally Confined Spaces. *ACS Omega* **2019**, *4*, 13106−13113.
(72) Varadharajan, D.; Turgut, H.; Lahann, J.; Yabu, H.; Delaittre, G. Surface-Reactive Patchy Nanoparticles and Nanodiscs Prepared by Tandem Nanoprecipitation and Internal Phase Separation. *Adv. Funct. Mater.* **2018**, *28*, 1800846.
(73) Yabu, H.; Higuchi, T.; Ijiro, K.; Shimomura, M. Spontaneous formation of polymer nanoparticles by good-solvent evaporation as a nonequilibrium process. *Chaos* **2005**, *15*, 047505.
(74) Higuchi, T.; Pinna, M.; Zvelindovsky, A. V.; Jinnai, H.; Yabu, H. Multipod structures of lamellae-forming diblock copolymers in three-dimensional confinement spaces: Experimental observation and computer simulation. *J. Polym. Sci., Part B: Polym. Phys.* **2016**, *54*, 1702−1709.
(75) Higuchi, T.; Motoyoshi, K.; Sugimori, H.; Jinnai, H.; Yabu, H.; Shimomura, M. Three-dimensional observation of confined phase-separated structures in block copolymer nanoparticles. *Soft Matter* **2012**, *8*, 3791−3797.
(76) MessaoudiI, C.; Boudier, T.; Sorzano, C. O. S.; Marco, S. TomoJ: tomography software for three-dimensional reconstruction in transmission electron microscopy. *BMC Bioinf.* **2007**, *8*, 288.
(77) Miyake, A.; Matsuno, J.; Toh, S. Sample preparation toward seamless 3D imaging technique from micrometer to nanometer scale. *Microscopy* **2014**, *63*, i24−i25.
(78) Eyre, D. J. An Unconditionally Stable One-Step Scheme for Gradient Systems. *IEEE Trans. Image Process.* **1997**.
(79) Teramoto, T.; Nishiura, Y. Morphological characterization of the diblock copolymer problem with topological computation. *Jpn. J. Ind. Appl. Math.* **2010**, *27*, 175−190.

https://doi.org/10.1021/acsomega.3c10302
ACS Omega 2024, 9, 17276−17288